








Article

Influence of the clay fractions from various horizons on the radiation shielding parameters of an Arenosol

Luiz F. Pires^{1*} , Victor A. Yanaguisawa² , André M. Brinatti¹ , Sérgio C. Saab¹  and Vladia Correchel³ 

¹Department of Physics, State University of Ponta Grossa (UEPG), Ponta Grossa, Brazil; ²Physics Graduate Program, State University of Ponta Grossa (UEPG), Ponta Grossa, Brazil and ³School of Agronomy, Federal University of Goiás (UFG), Goiânia, Brazil

Abstract

This study examines the effects of the chemical composition of the clay fraction of various soil horizons on radiation shielding parameters. X-ray fluorescence (XRF) analysis did not reveal significant differences in the concentration of the most abundant oxides (Al_2O_3 , SiO_2 , Fe_2O_3) among the various horizons. Consequently, the mass attenuation coefficient did not vary among the horizons in terms of the photon energies studied (15 keV–10 MeV). The mean free path (MFP), half-value layer (HVL) and tenth-value layer (TVL) did not differ for energies up to 100 keV. However, at higher energies, these parameters were mainly influenced by the differences in the densities of the soil horizons. The effective atomic number did not differ across the horizons for the various photon energies, nor did the mass attenuation coefficient. It is shown that slight differences in the chemical composition of the clay fraction of soil horizons do not affect radiation shielding parameters (MFL, HVL, TVL) for low photon energies (<500 keV). Density is more important for radiation shielding than the chemical composition of the various horizons of the same soil type for higher energies (>100 keV); hence, compacting the clay fraction might be more efficient for radiation shielding purposes at higher energies.

Keywords: Half-value layer, mean free path, *Phy-X/PSD*, soil, tenth-value layer, *XCOM*

(Received 10 November 2023; revised 19 February 2024; Associate Editor: Hongping He)

Soil is a widely available material on Earth and is recognized as a cost-effective and accessible natural resource for radiation shielding purposes (Akman *et al.*, 2019). There are several effective shielding materials, several of which are costly and potentially hazardous, such as heavy metals (AbuAlRoos *et al.*, 2019). When a soil is used as a shielding material, the clay fraction can prove particularly advantageous due to the reactive nature of its particles, facilitating the formation of cohesive structures (aggregates; Schaefer *et al.*, 2008). Soil horizons exhibit variability in their physical and chemical properties influenced by the texture, chemical and mineralogical composition and type of the parent rock, among other factors (Hartemink *et al.*, 2020). Thus, from an environmental perspective, determining the shielding capacity of distinct soil horizons against radiation is crucial.

Numerous studies have confirmed the feasibility of depositing radioactive waste in natural sites, highlighting the importance of investigating the efficacy of various soil layers (horizons) for attenuating radiation (Delage *et al.*, 2010; Tsang *et al.*, 2015; Eke, 2022). It has been demonstrated that several dozen centimetres of natural materials, such as soil and clays, can efficiently attenuate gamma ray photons of various energies (Mann *et al.*, 2016; Mamikhin *et al.*, 2017).

Several parameters are used to evaluate the shielding ability of various materials. The linear (κ) and mass (μ) attenuation coefficients are essential parameters that enable the determination of

the probability that a photon will be attenuated (Hubbell & Seltzer, 1995). Another highly influential parameter is the mean free path (MFP), which indicates the average distance a photon can travel in a specific material before experiencing a collision (Alabsy & Elzaher, 2023). Overall, the MFP offers an objective measure of the probability that a given interaction between photons and matter will occur. In addition, two commonly employed parameters are the half-value layer (HVL) and the tenth-value layer (TVL), which represent the thickness of material required to reduce the radiation intensity by a factor of one-half and one-tenth, respectively, of the initial intensity (Alabsy & Elzaher, 2023). The effective atomic number (Z_{eff}) is another parameter commonly used in radiation physics due to its importance in calculating the absorbed dose of radiation (Alabsy & Elzaher, 2023). This parameter is used when materials composed of many chemical elements are analysed, such as the clay fraction of the soil.

Different techniques can be used in radiation shielding, which can be based on experimental measurements and computer simulation. These techniques allow numerous parameters to be obtained, the most common being attenuation coefficient data, cross-sections (σ), Z_{eff} , electronic density (N_{eff}), energy absorption and exposure build-up factors (EABF, EBF), effective conductivity (C_{eff}), MFP, HVL, TVL and fast neutron removal cross-section (FNRCs; Şakar *et al.*, 2020). The attenuation coefficients, MFP, HVL, TVL and Z_{eff} are commonly found in the literature (Abdul & Rashid, 2021; Eke, 2021; Marquez-Mata *et al.*, 2021; Gili, 2023). Thus, our study used the radiation shielding parameters most commonly employed in the scientific literature. For a detailed description of radiation shielding techniques and

*Email: lppires@uepg.br

Cite this article: Pires LF, Yanaguisawa VA, Brinatti AM, Saab SC, Correchel V. Influence of the clay fractions from various horizons on the radiation shielding parameters of an Arenosol. *Clay Minerals*. <https://doi.org/10.1180/clm.2024.16>

the advantages and limitations of each method, we recommend the review article by Shultis & Faw (2005).

Previous studies have examined soil and clays as potential radiation shielding materials (Kucuk *et al.*, 2013; Mann *et al.*, 2013; Akman *et al.*, 2019; Isfahani *et al.*, 2019a; Hila *et al.*, 2021). However, these studies usually analyse one unique layer and the soil as a whole rather than its fractions, such as the highly reactive clay fraction (Medhat *et al.*, 2014a; Singh *et al.*, 2014; Mamikhin *et al.*, 2017). As the various soil horizons may differ in the chemical compositions of their clay fractions, thus affecting radiation attenuation (Gedik & Baytaş, 2015; Pires, 2022), collecting soil samples along the soil profile is necessary to assess how each layer influences radiation shielding.

This study is based on the hypothesis that the various horizons, with slight differences between their mineral compositions and soil bulk densities, show variations in shielding parameters in terms of the various photon energies based on analysis of their soil clay fractions. The study aimed to characterize the chemical composition of the clay fractions in various horizons of an Arenosol and evaluate the efficiency of these horizons for shielding radiation. Additionally, the study aimed to observe the variations of the shielding parameters depending on the photon energy. A schematic illustration of the research steps is presented in Fig. S1.

The main advance of this study regarding the area of radiation shielding is the analysis of the clay fractions of various soil horizons. This type of investigation can provide information on the efficiency of each soil layer for attenuating radiation. The study also evaluates the clay fraction obtained through physical fractionation of the soil rather than clays composed of single minerals. In general, studies on radiation shielding in the scientific literature focus on pure clays. Using the clay fraction obtained directly from the soil could be an alternative for producing low-cost materials for radiation shielding.

Materials and methods

Soil sampling and soil preparation

The studied soil was collected from the profile located at coordinates 16°30'27" S and 52°22'29" W, with a local average elevation of 565 m, in the municipality of Baliza in the state of Goiás, Brazil (Fig. 1). This soil was identified as an Arenosol according to the IUSS Working Group WRB (2022) classification system. The soil comprises five horizons (Table 1).

The samples were air-dried at 40°C and passed through a 2 mm mesh sieve to obtain air-dried fine earth (ADFE). The silt and clay fractions of the ADFE were separated using NaOH (1 mol L⁻¹), with the sand fraction (2 mm to 53 µm) separated by sieving. The silt and clay fractions were physically fractionated according to Stokes' law (Gee & Bauder, 1986). The particle density of the ADFE was determined using a He gas pycnometer, ranging from 2.60 to 2.62 g cm⁻³.

The clay fraction was separated from the water with the addition of CaCl₂ (1 mol L⁻¹). Once obtained, the clay fraction was dried at 40°C, ground with a pestle and mortar and sieved through a 45 µm sieve. The soil texture (Fig. 2) was determined using the pipette method according to the procedure outlined in Tech *et al.* (2022).

X-ray diffraction and X-ray fluorescence analysis

X-ray diffraction (XRD) measurements of the clay fraction were obtained from one sample from each portion. The samples were

placed in the sample holder and gently pressed with a glass slide to fix them in place. The XRD analysis was carried out using an Ultima IV diffractometer from Rigaku, Cu-K α radiation, 40 kV, 30 mA, in the range 3–100°2 θ , with a 0.02°2 θ scanning step and a time of 5 s per step. The slit settings used were as follows: 10 mm horizontal divergence slit, 1° scatter slit and 0.15 mm receiving slit. The XRD traces were compared with the standard mineral patterns of the Mineralogy Database (<https://www.webmineral.com/>) and the American Mineralogist Crystal Structure Database (<http://rruff.geo.arizona.edu/AMS/amcsd.php>). This comparison was carried out by considering at least the three most intense diffraction peaks of each mineral, the corresponding interlayer spacing and the peak position for Cu-K α radiation (Prandel *et al.*, 2014).

The chemical composition of the clay fractions in each horizon was determined semi-quantitatively using energy-dispersive X-ray fluorescence (EDXRF). Na to Sc were determined at 5 kV and Ti to U were determined at 50 kV, using ~1 g of powder samples. The samples were dried at 40°C, ground with a pestle and mortar, sieved through a 45 µm sieve and placed into sample holders. The measurements were carried out using a benchtop XRF spectrometer (EDX-720, Shimadzu) with a Si(Li) semiconductor system detector cooled with liquid N at -196°C (Ferreira *et al.*, 2018).

Calculation of shielding parameters

The XCOM (Hubbell & Berger, 1987) and Phy-X/PSD (Şakar *et al.*, 2020) programs were used to calculate the mass attenuation coefficient. These programs can analyse both pure and compound elements, such as soil clay fractions composed of several chemical elements. For this study, the photon energy range selected was 15 keV to 10 MeV. This range was chosen to verify the attenuation efficiency of the clay fraction for low (15 and 50 keV), intermediate (100 keV to 1 MeV) and high (>1 MeV) energy levels. The mass attenuation coefficient of a compound or a mixture can be obtained using the formula given in Equation 1 (Hubbell & Berger, 1987):

$$\mu = \sum_i W_i \mu_i \quad (1)$$

where μ_i is the mass attenuation coefficient of the i th term and W_i is the weight fraction.

Based on the soil bulk density (ρ_b) results, the linear attenuation coefficient of the clay fraction was calculated. Soil bulk density was determined using sieved soil samples placed in volumetric flasks with a volume of ~17.7 cm³. The flasks were carefully filled with a funnel using small vibrations. The filling procedure followed is similar to that used in κ measurements according to the gamma-ray attenuation method (Costa *et al.*, 2014). The ρ_b values obtained for the various horizons are listed in Table 1. Multiplying μ by ρ_b enabled calculation of κ , which is related to the probability of a photon being attenuated or absorbed per unit length.

The MFP, which measures the average distance travelled by a particle before it collides with another particle, was calculated using the relationship given in Equation 2 (Şakar *et al.*, 2020):

$$\text{MFP} = \frac{\int_0^{\infty} x e^{-\kappa x} dx}{\int_0^{\infty} e^{-\kappa x} dx} = \frac{1}{\kappa} \quad (2)$$

where x represents the thickness of the absorber material.

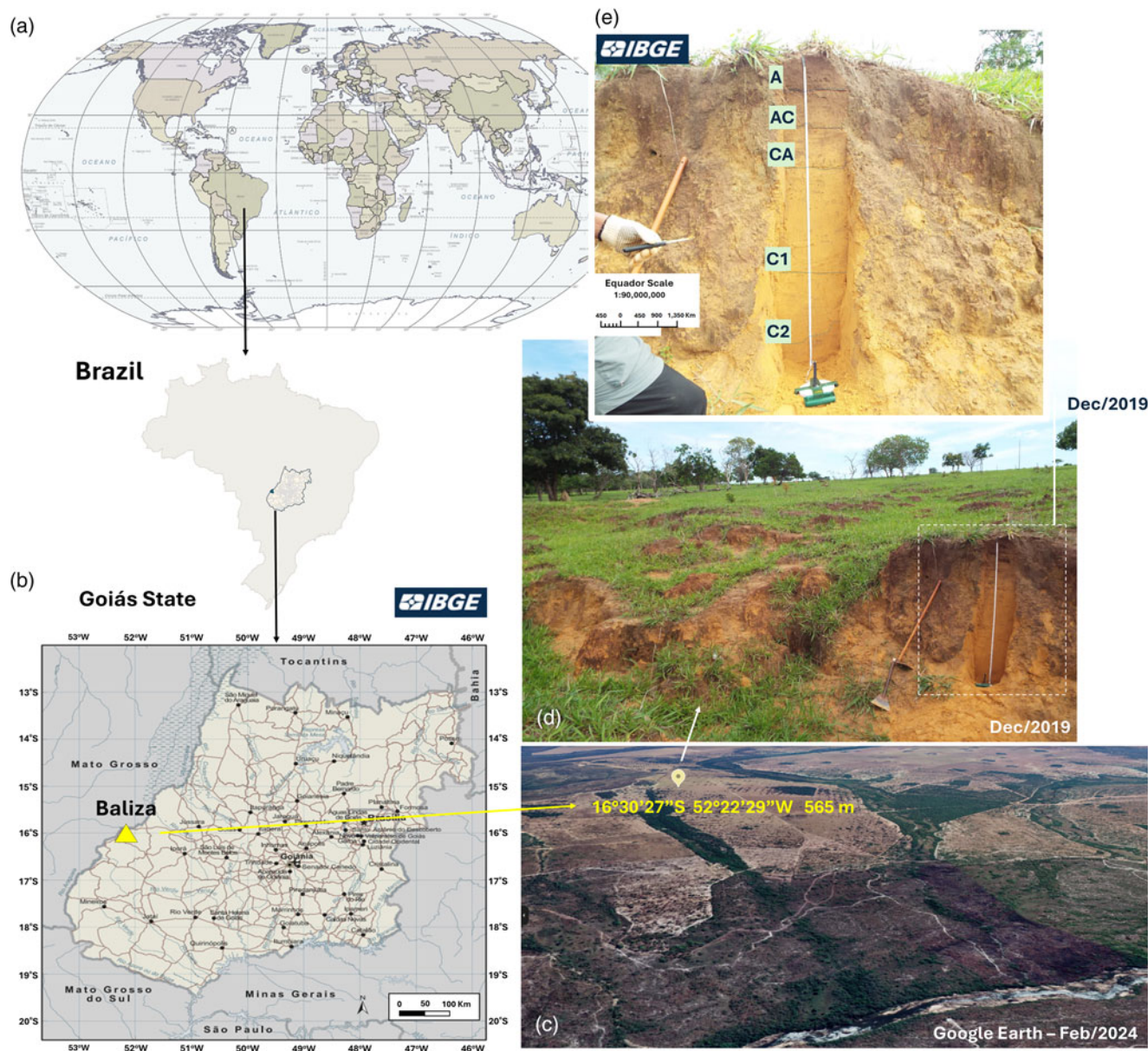


Figure 1. (a,b) Location of the studied experimental site (Baliza, state of Goiás, Brazil) (adapted from the Brazilian Institute of Geography and Statistics (IBGE)). (c) Aerial view of the area (accessed from Google Earth on 10 February 2024). (d) Photograph of the experimental area. (e) Photograph of the Arenosol soil profile (horizons A, AC, CA, C1 and C2).

The HVL and TVL were calculated according to Equations 3 & 4 (Şakar *et al.*, 2020):

$$\text{HVL} = \frac{\ln(2)}{\kappa} = \frac{0.693}{\kappa} \quad (3)$$

$$\text{TVL} = \frac{\ln(10)}{\kappa} = \frac{2.302}{\kappa} \quad (4)$$

Table 1. Description of the soil horizons and the soil bulk densities (ρ_b) of the studied Arenosol.

	A	AC	CA	C1	C2
Depth (cm)	0–21	21–42	42–65	65–125	>125
ρ_b (g cm ⁻³)	1.49	1.43	1.41	1.43	1.47

The effective atomic number was calculated from the ratio between the atomic (σ_a) and electronic (σ_e) cross-sections as per Equation 5 (Şakar *et al.*, 2020):

$$Z_{\text{eff}} = \frac{\sigma_a}{\sigma_e} \quad (5)$$

The atomic cross-section was obtained from division of the molecular cross-section (σ_m) by the total number of formula units as per Equation 6 (Medhat *et al.*, 2014b):

$$\sigma_a = \sigma_m \frac{1}{\sum_i n_i} \quad (6)$$

where $\sum n_i$ is the total number of formula units of the compound. ⁱThe molecular cross-section was calculated as per Equation 7 (Medhat *et al.*, 2014b):

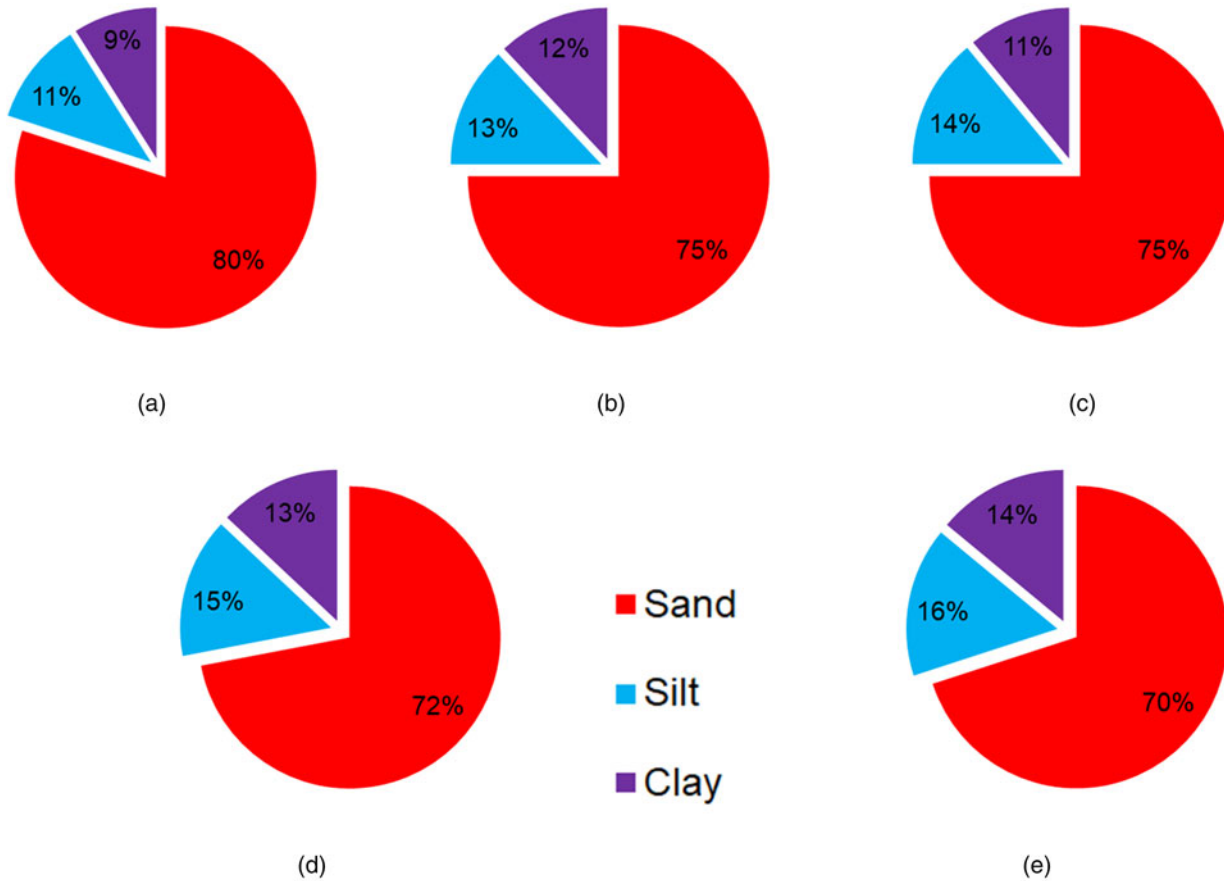


Figure 2. Percentages of sand, silt and clay in the studied Arenosol for the various horizons: (a) A, (b) AC, (c) CA, (d) C1 and (e) C2.

$$\sigma_m = \mu \frac{M}{N_A} \quad (7)$$

where $M = \sum_i n_i A_i$ is the molecular weight of the compound, N_A is the Avogadro number, A_i is the atomic weight of the i th element and n_i is the number of formula units in the molecule. The total electronic cross-section was obtained using Equation 8 (Medhat *et al.*, 2014b):

$$\sigma_e = \frac{1}{N_A} \sum_i f_i \frac{A_i}{Z_i} \mu_i \quad (8)$$

where $f_i = \frac{n_i}{\sum_j n_j}$ and Z_i are the fractional abundance and the atomic number of the i th constituent element, respectively, n_j is the number of atoms of the constituent element and $\sum_j n_j$ is the total number of atoms present in the molecular formula.

Statistical analysis

Analysis of variance (ANOVA) was used to compare the results among the various soil horizons regarding their chemical compositions and mass attenuation coefficients. The normality and equal variance assumptions were checked using the Shapiro–Wilk and Bartlett tests, respectively. Once these assumptions were confirmed, the F -test was employed. When significant interactions were found, Tukey’s test was used for post-hoc comparisons.

Furthermore, Pearson’s linear correlation analysis was conducted to assess possible correlations among the measured parameters. The MFP, HVL, TVL and Z_{eff} parameters were analysed based on the average values and standard deviation. The statistical data processing was performed using the *Past* program (version 3.20), as described by Hammer *et al.* (2001).

Results

Mineralogical and chemical analysis

The XRD traces of the clay fractions of the soil samples are shown in Fig. 3. The clay fractions of all horizons were similar in terms of mineralogical composition, indicating a predominance of kaolinite (Kln; Bish & Von Dreele, 1989) and gibbsite (Gbs; Balan *et al.*, 2006). Other minerals present are calcite (Cal; Graf, 1961), quartz (Qz; Wei, 1935), anatase (An; Howard *et al.*, 1991) and magnetite (Mag; Wechsler *et al.*, 1984), with the latter two minerals being the main hosts of the Ti and Fe detected in the clay fractions.

No significant differences ($p > 0.05$) were found for the contents of Al_2O_3 , SiO_2 , Fe_2O_3 and SO_3 (Table 2). The first three oxides accounted for ~95% of the chemical composition of the clay fraction in the studied horizons. The variation in Al_2O_3 , SiO_2 and Fe_2O_3 between horizons ranged between ~3.8% (AC and C1), ~4.4% (A and C1) and ~9.9% (A and C1). CaO, K_2O and TiO_2 displayed significant differences ($p \leq 0.05$) between specific horizons (Table 2). However, their contribution ($\text{CaO} + \text{K}_2\text{O} +$

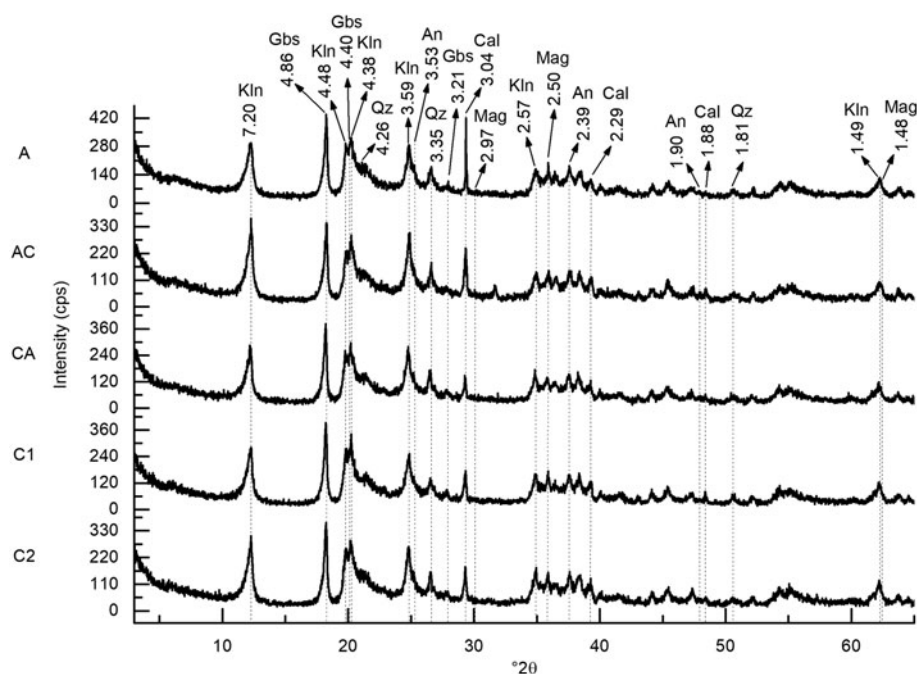


Figure 3. XRD traces of the clay fractions of the Arenosol for the various soil horizons (A, AC, CA, C1 and C2); *d*-spacings are in Ångströms (Å). An = anatase; Cal = calcite; cps = counts per second; Gbs = gibbsite; Kln = kaolinite; Mag = magnetite; Qz = quartz.

TiO₂) to the composition of the clay fraction was relatively low, ranging from ~4.8% (A) to ~5.8% (AC). Only those oxides with concentrations near or exceeding 1% are presented in Table 2. The full chemical composition of the soil clay fraction is listed in Table S1.

Radiation shielding parameters

No significant differences ($p > 0.05$) were observed in the mass attenuation coefficients between the different photon energy ranges analysed and among the soil horizons (Table 3). The most considerable variations were observed at lower energies (15 and 50 keV), between AC and C1, by ~3%. When analysing the partial effects of radiation attenuation (namely, photoelectric absorption, coherent scattering, incoherent scattering and pair production), it became evident that photoelectric absorption is responsible for the majority of photon attenuation at lower energies, accounting for ~95% of the total attenuation (Fig. 4). As photon energy increased to intermediate levels, incoherent scattering became the predominant contributor to photon attenuation, responsible for ~82% at 100 keV and virtually 100% at 1 MeV. However, at higher energies, nuclear field pair production was more significant, accounting for ~32% of the radiation attenuation (Fig. 4f). However, as observed for the μ values (Table 3), there were no differences in the contributions of the

Table 3. Average values of the mass attenuation coefficients for the various soil horizons (A, AC, CA, C1 and C2) and photon energies (E).

Horizon	Photon energy (MeV)					
	0.015	0.05	0.1	0.5	1	10
A	7.6 (0.1) ^a	0.39 (0.02) ^a	0.176 (0.002) ^a	0.086 (-)	0.063 (-)	0.023 (-)
AC	7.7 (0.2) ^a	0.39 (0.02) ^a	0.176 (0.003) ^a	0.086 (-)	0.063 (-)	0.023 (-)
CA	7.6 (0.1) ^a	0.39 (0.02) ^a	0.176 (0.003) ^a	0.086 (-)	0.063 (-)	0.023 (-)
C1	7.5 (0.1) ^a	0.38 (0.02) ^a	0.175 (0.003) ^a	0.086 (-)	0.063 (-)	0.023 (-)
C2	7.6 (0.1) ^a	0.38 (0.01) ^a	0.174 (0.001) ^a	0.086 (-)	0.063 (-)	0.023 (-)

Notes: The values in parentheses represent the standard deviation of the average ($n = 3$). (-) indicates a standard deviation much smaller than the last significant figure of the average value. Superscript letters indicate significant differences between soil horizons in terms of the photon energy in question ($p < 0.05$). The statistical test was not applied for energies greater than 100 keV due to the lack of variability between the mass attenuation coefficient results among horizons.

partial attenuation effects between the horizons of the clay fraction studied.

Given the deviations (error bars) from the average values, the MFP differences were less noticeable for the lowest photon energies (15 and 50 keV; Fig. 5a,b). However, as photon energy increased (>50 keV), the differences between the soil horizons became more apparent (Fig. 5c-f). The intermediate horizon (CA) displayed the greatest average MFP value, while the surface horizon (A) displayed the lowest average MFP value. The range of

Table 2. Average values of the chemical compositions of the clay fractions of the soil horizons (A, AC, CA, C1 and C2) of the studied Arenosol.

Horizon	Oxides (wt.%)						
	Al ₂ O ₃	SiO ₂	CaO	Fe ₂ O ₃	SO ₃	K ₂ O	TiO ₂
A	57.7 (0.6) ^a	32.9 (0.5) ^a	2.1 (0.1) ^c	4.4 (0.3) ^a	0.7 (0.1) ^a	1.1 (-) ^b	0.9 (0.1) ^{ab}
AC	57.3 (0.9) ^a	32.7 (0.5) ^a	3.3 (0.1) ^a	4.1 (0.2) ^a	0.5 (-) ^a	1.1 (-) ^b	0.9 (0.1) ^{ab}
CA	58.4 (0.9) ^a	32.5 (0.3) ^a	2.1 (0.1) ^c	4.3 (0.2) ^a	0.6 (0.1) ^a	1.1 (-) ^{ab}	1.0 (0.1) ^{ab}
C1	59.5 (1.1) ^a	31.5 (1.0) ^a	2.5 (-) ^b	4.0 (-) ^a	0.5 (0.1) ^a	1.0 (-) ^b	0.8 (0.1) ^b
C2	57.7 (0.8) ^a	32.8 (0.4) ^a	2.3 (0.1) ^c	4.3 (0.3) ^a	0.6 (0.1) ^a	1.2 (-) ^a	1.0 (-) ^a

Notes: Only the oxides with the highest concentrations are shown. The values in parentheses represent the standard deviation of the average ($n = 3$). (-) indicates a standard deviation much smaller than the last significant figure of the average value. The superscript letters indicate significant differences between the soil horizons in terms of the oxide in question ($p < 0.05$).

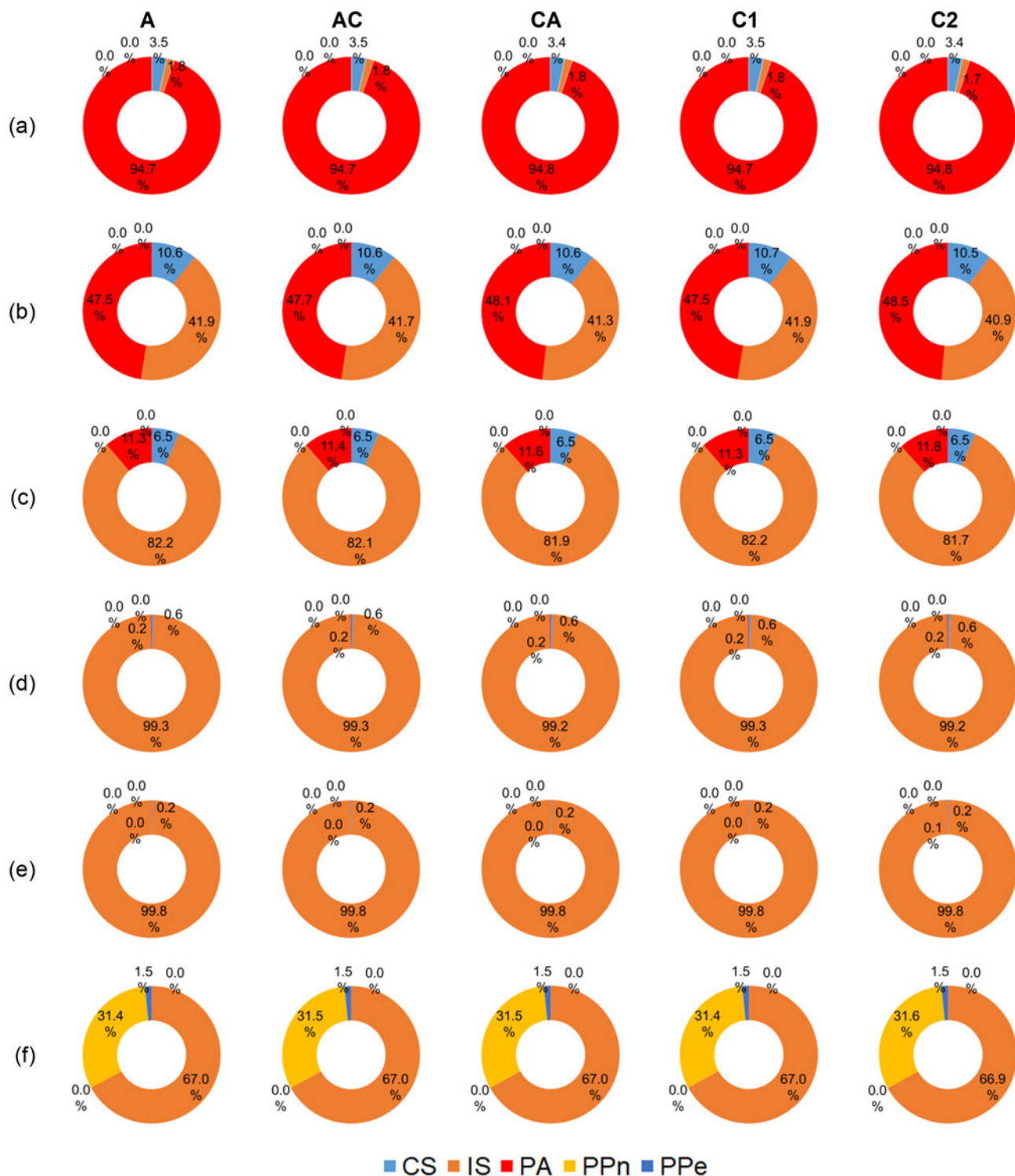


Figure 4. Contributions of partial effects (photoelectric absorption (PA), coherent scattering (CS), incoherent scattering (IS) and pair production (PP)) to the total attenuation coefficients (μ) for photon energies of (a) 15 keV, (b) 50 keV, (c) 100 keV, (d) 500 keV, (e) 1 MeV and (f) 10 MeV. A, AC, CA, C1 and C2 represent the various Arenosol horizons. PPn = pair production in a nuclear field; PPe = pair production in an electron field.

MFP values between the horizons (A and CA) varied by $\sim 5.4\%$ (15 keV to 10 MeV). When accounting for the different photon energies, the MFP (average values considering all of the horizons) ranged from ~ 0.091 cm (15 keV) to 30.51 cm (10 MeV).

Similarly to MFP, lower photon energies (15 and 50 keV) exhibited more subtle differences in the HVL (Fig. 6a,b) and

TVL (Fig. 7a,b). Nonetheless, as photon energy increased (>50 keV), both HVL (Fig. 6c–f) and TVL (Fig. 7c–f) exhibited more pronounced differences (based on error bars) among the studied horizons. The surface horizon (A) demonstrated the lowest average values of both parameters, while the CA horizon exhibited the highest values. In accordance with MFP, the

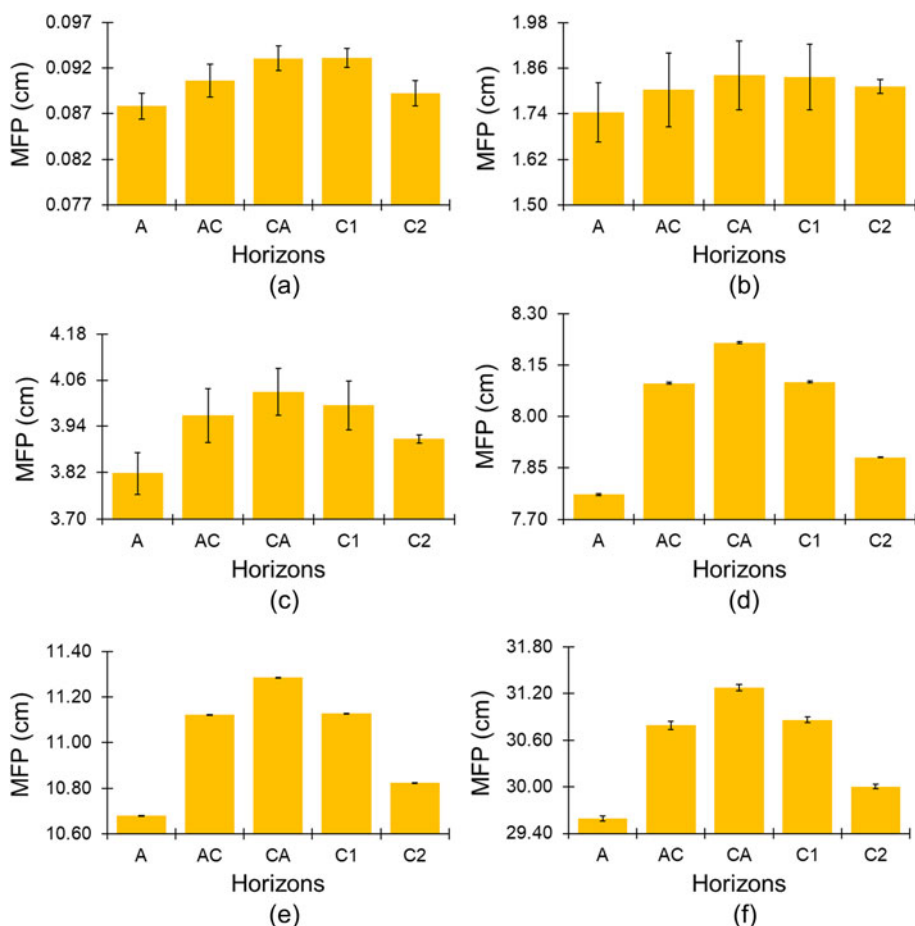


Figure 5. Variation in the MFP values for the various horizons (A, AC, CA, C1, C2) of the Arenosol studied for the photon energies of (a) 15 keV, (b) 50 keV, (c) 100 keV, (d) 500 keV, (e) 1 MeV and (f) 10 MeV.

difference between the highest and lowest HVL and TVL average values for the horizons (A and CA) was $\sim 5.4\%$ (50 keV to 10 MeV). Considering the different photon energies, the HVL and TVL (average values considering all of the horizons) ranged from ~ 0.063 cm (15 keV) to 21.14 cm (10 MeV) and from 0.21 cm (15 keV) to 70.24 cm (10 MeV), respectively.

The effective atomic number showed slight differences among the soil horizons considering the average values and their deviations (error bars) for the various photon energies examined (Fig. 8). Generally, the Z_{eff} average values were similar across horizons for the various energies, with the AC horizon having the greatest Z_{eff} value. Among the photon energies, the lowest one (15 keV) had the greatest Z_{eff} values, averaging ~ 14.5 (Fig. 8a). The Z_{eff} value demonstrated a noticeable decrease with energy increasing up to 1 MeV, averaging ~ 10.3 . It then showed a slight increase up to 10 MeV, averaging ~ 10.6 (Fig. 8e,f). The most significant decrease in Z_{eff} was recorded between the energies of 50 keV (Fig. 8b) and 100 keV (Fig. 8c), where it decreased up to $\sim 14.4\%$.

Discussion

This study aimed to verify the efficiency of the clay fractions from various horizons (with slight differences in their mineralogical compositions) to shield photons of various energies. The clay fraction used was selected as it is possible to be mixed with other materials (e.g. concrete and metal) to produce radiation shielding materials (Akbulut *et al.*, 2015; Isfahani *et al.*, 2019a).

Clay also has a high capacity to form soil aggregates; hence, it might be used as a shielding material due to its ability to produce soil aggregates that are relatively stable and have a strong structure (Hillel, 2014; Mann *et al.*, 2016).

The soil texture results (Fig. 2) show that the clay fraction varied from 9% (A horizon) to 14% (C2 horizon). The soil studied mainly consists of sand, ranging from 80% (A) to 70% (C2). The soil composition aligns with the Arenosols found in Brazil (Oliveira *et al.*, 2016; Silva *et al.*, 2017), with the texture classified as loamy sand in the most superficial horizon (A) and sandy loam in the remaining horizons. The clay fraction is mainly composed of Al_2O_3 and SiO_2 (Table 2), the most abundant Arenosol oxides (Ngole-Jeme & Ekosse, 2015). The mineralogical composition of the clay fraction is in agreement with other Arenosols (Mareschal *et al.*, 2011; Bortoluzzi *et al.*, 2013; dos Santos *et al.*, 2017; Lima *et al.*, 2022; Zacháry *et al.*, 2023).

Due to the slight variations in the contents of the major oxides (Al_2O_3 , SiO_2 and Fe_2O_3) present in the clay fractions, no differences were observed in the mass attenuation coefficients (Table 3) for the various photon energies between the various horizons. The μ values are comparable to previous studies on soils, clays or sands (Medhat *et al.*, 2014a; Eke, 2021; Pires, 2022; Gili, 2023). As photon energy increases, μ values decrease, similar to that which has been observed in previous work (Singh *et al.*, 2014; Gurler *et al.*, 2021; Gili, 2023). Analysing the partial attenuation effects, it can be observed that photoelectric absorption is prevalent at lower energies (Fig. 4a,b), as it depends on Z^5 (Camargo *et al.*, 2021). However, with increasing

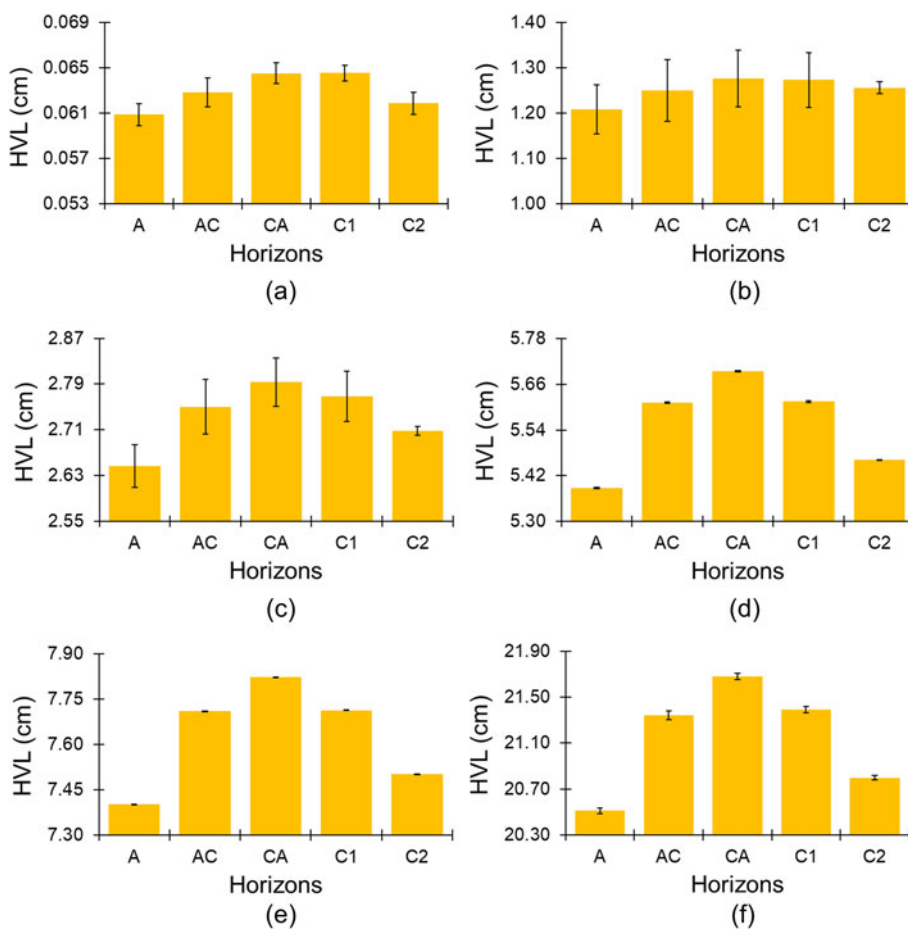


Figure 6. Variation in the HVL values for the various horizons (A, AC, CA, C1, C2) of the Arenosol studied for the photon energies of (a) 15 keV, (b) 50 keV, (c) 100 keV, (d) 500 keV, (e) 1 MeV and (f) 10 MeV.

energy levels, photoelectric absorption becomes less critical due to its inverse dependence on photon energy ($E^{7/2}$; Kaplan, 1963). For intermediate energy levels (Fig. 4c–e), incoherent scattering is the predominant process affecting photon attenuation. This effect is directly proportional to Z (Camargo *et al.*, 2021). For higher energies (Fig. 4f), pair production (i.e. when an electron–positron pair is formed after a photon with an energy of 1.022 MeV or more interacts with an atom’s nuclear force field) contributes more significantly to the photon attenuation, which is related to the dependence of this effect on Z^2 (Camargo *et al.*, 2021). Overall, the similarities in the contribution of partial effects (i.e. photoelectric absorption, coherent scattering, incoherent scattering and pair production) to the total mass attenuation coefficient can be explained by slight variations in the chemical compositions of the clay fractions between horizons, particularly for the heavier chemical elements (Camargo *et al.*, 2021; Pires, 2022).

The parameters for MFP (Fig. 5), HVL (Fig. 6) and TVL (Fig. 7) showed slight variations among the horizons for the lowest photon energies (15 and 50 keV) considering the deviations (error bars) of the average values. The horizons with the highest bulk densities (A and C2) had the lowest MFP, HVL and TVL values, even at the lowest energies (except for 50 keV). Nevertheless, as the photon energy increased (>50 keV), the differences in MFP (Fig. 5c–f), HVL (Fig. 6c–f) and TVL (Fig. 7c–f) between the various horizons became more pronounced. This result does not indicate that the proportional differences between these parameters’ highest and lowest values across the horizons have changed considering the various photon energies. These differences remain practically the same (~5.4%),

but the average values’ deviations (error bars) become negligible for the higher energies. One possible explanation for these findings is that MFP, HVL and TVL values converge at greater photon energies due to the weaker attenuation caused by the absorber, resulting in reduced variability (Table 3). Inasmuch as the horizons have comparable chemical compositions, the differences in MFP, HVL and TVL were mainly influenced by the bulk density values of the absorber. Horizon (A), with the greatest bulk density, displayed the lowest MFP, TVL and HVL values, whereas horizon (CA), with the lowest bulk density, exhibited the highest MFP, TVL and HVL values. Eke (2022) also observed more significant variation in MFP, HVL and TVL between various soil layers (horizons) at the greatest photon energies for soils composed mainly of Ca and O, similar to the findings observed in our study.

The linear attenuation coefficient is affected by the soil bulk density, as previously stated. Thus, an increase in ρ_b leads to an increase in κ , assuming that the chemical composition of the material and the photon energy remain constant (Ferraz & Mansell, 1979). The parameters MFP, HVL and TVL are inversely related to κ (Equations 2–4). In general, samples with higher ρ_b exhibited lower MFP (Fig. 5), HVL (Fig. 6) and TVL values (Fig. 7). In this study, κ , obtained by multiplying μ by ρ_b , and μ , which varied depending on the chemical composition of the soil, influenced the MFP, HVL and TVL parameters.

The MFP, HVL and TVL values observed were consistent with those reported in the literature (i.e. they increased with increasing photon energy; Gülbicim *et al.*, 2017; Isfahani *et al.*, 2019a; Eke, 2022). The MFP values were comparable to those observed by

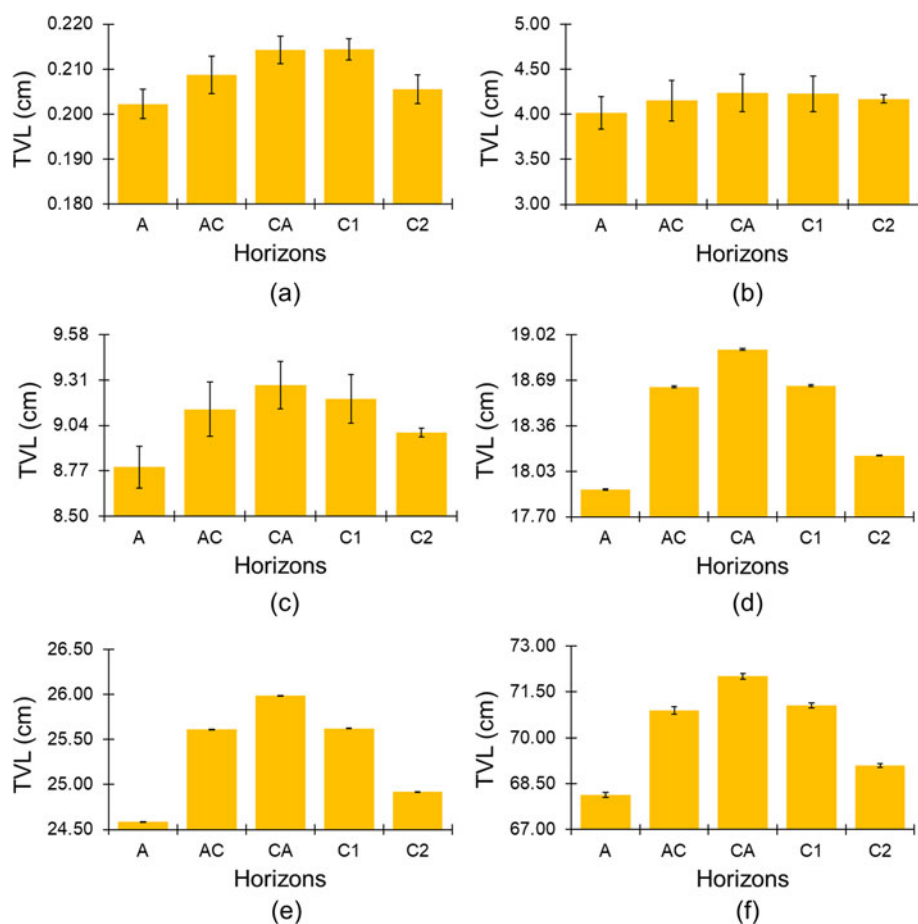


Figure 7. Variation in the TVL values for the various horizons (A, AC, CA, C1, C2) of the Arenosol studied for the photon energies of (a) 15 keV, (b) 50 keV, (c) 100 keV, (d) 500 keV, (e) 1 MeV and (f) 10 MeV.

Eke (2021), although Eke reported slightly lower values than those in the current study due to the greater density of the analysed sands. However, in another study conducted with soils, Eke (2022) reported MFP values similar to those observed in our study. Our HVL values are consistent with those of Singh *et al.* (2014), who worked with various soils with densities similar to ours; Gurler *et al.* (2020), who analysed soils with similar amounts of Fe_2O_3 to those observed in our study; and Gülbiçim *et al.* (2017), who investigated the efficiency of vermiculite in radiation shielding. Regarding the study by Gülbiçim *et al.* (2017), their MFP and HVL values were lower than those observed in the current study as they only used a single type of clay. The TVL values obtained were consistent with those obtained in similar studies that used clays and soils of comparable chemical composition (i.e. consisting mainly of SiO_2 , Al_2O_3 and Fe_2O_3 ; Isfahani *et al.*, 2019b; Gurler *et al.*, 2020; Pires, 2022).

The optimum values for horizon (A), with the best shielding results for MFP, can be defined as a function of photon energy as 0.088 cm (15 keV), 1.74 cm (50 keV), 3.82 cm (100 keV), 7.77 cm (500 keV), 10.68 cm (1 MeV) and 29.59 cm (10 MeV). The same horizon exhibited the greatest shielding capacity according to the HVL and TVL results. The HVL values obtained were 0.061 cm (15 keV), 1.21 cm (50 keV), 2.65 cm (100 keV), 5.39 cm (500 keV), 7.40 cm (1 MeV) and 20.51 cm (10 MeV), whereas for TVL the values recorded were 0.202 cm (15 keV), 4.02 cm (50 keV), 8.79 cm (100 keV), 17.90 cm (500 keV), 24.59 cm (1 MeV) and 68.14 cm (10 MeV).

The effective atomic number showed slight differences between the horizons and the various photon energies in terms of average values and the corresponding standard deviations (error bars; Fig. 8). The results of this study are consistent with those in the literature for soil and clay samples (Akman *et al.*, 2019; Marquez-Mata *et al.*, 2021; Gili, 2023). The fluctuations observed in Z_{eff} values with energy were also reported for zeolites (Gili, 2023), soils of various textures (Kucuk *et al.*, 2013) and various types of natural quartz (Marquez-Mata *et al.*, 2021). Thus, although natural materials such as clays and quartz have distinct chemical compositions, they are mainly composed of light elements (low Z), so the Z_{eff} values are similar to those in the current study.

Horizon (AC) exhibited the greatest Z_{eff} values for all of the analysed photon energies. One possible explanation for this is the greater concentration of CaO and Fe_2O_3 (7.4% in total) encountered in this layer (Al-Masri *et al.*, 2013; Taqi & Khalil, 2017; Camargo *et al.*, 2022). The importance of Fe and Ca oxides to attenuating radiation in soils, especially for lower photon energies, has been well demonstrated (Mudahar *et al.*, 1991; Al-Masri *et al.*, 2013; Tarim *et al.*, 2013; Taqi & Khalil, 2017; Camargo *et al.*, 2021). In addition, soils with greater Ca contents had higher Z_{eff} values (Eke, 2022), which is in accord with the findings from the current study. The remaining horizons have comparable CaO and Fe_2O_3 contents; hence, the differences in the abundances of the remaining elements across photon energies may explain the differences between these horizons. In addition, the minor differences in the Fe_2O_3 contents observed between horizons may explain the similar Z_{eff} values (Table 3).

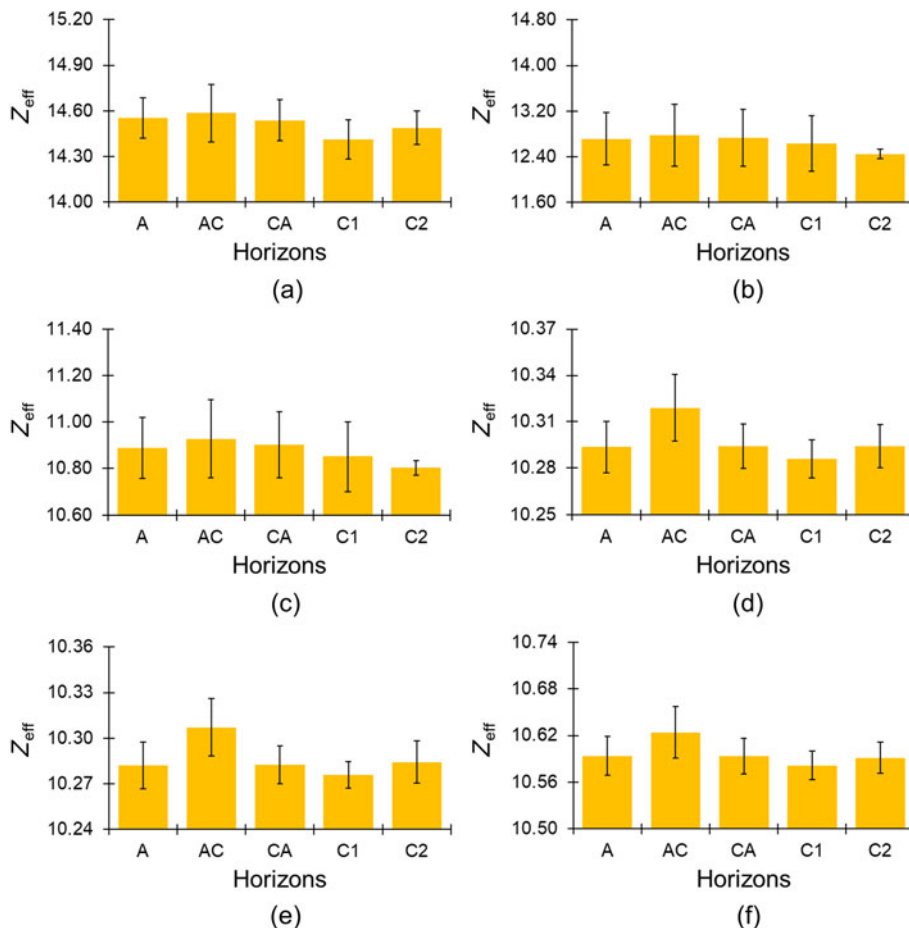


Figure 8. Variation in the effective atomic number (Z_{eff}) for the various horizons (A, AC, CA, C1, C2) of the Arenosol studied for the photon energies of (a) 15 keV, (b) 50 keV, (c) 100 keV, (d) 500 keV, (e) 1 MeV and (f) 10 MeV.

Azreen *et al.* (2018) analysed two types of concrete made from silica sand and lead glass and reported μ , HVL and TVL values of $0.065 \text{ cm}^2 \text{ g}^{-1}$, 2.56 cm and 4.17 cm, respectively, for the silica sand concrete and $0.071 \text{ cm}^2 \text{ g}^{-1}$, 2.44 cm and 4.05 cm, respectively, for the lead glass. Gili (2023) analysed natural zeolite and reported a μ value of $0.077 \text{ cm}^2 \text{ g}^{-1}$ and a HVL value of 8.05 cm. Isfahani *et al.* (2019b) recorded HVL and TVL values ranging from 3.53 to 4.96 cm (HVL) and from 11.74 to 16.47 cm (TVL) for clays modified with barite powder. Working with clay fly ash bricks, Mann *et al.* (2016) found μ values ranging from 0.0757 to $0.0789 \text{ cm}^2 \text{ g}^{-1}$. The Z_{eff} reported in the aforementioned works ranged from 10.73 to 11.85. Mirji & Lobo (2017) reported μ , HVL and TVL values ranging from 0.079 to $0.088 \text{ cm}^2 \text{ g}^{-1}$, from 3.78 to 8.37 cm and from 12.54 to 27.76 cm, respectively, for polymeric materials of various compositions. The shielding parameters of all of these studies were obtained for the ^{137}Cs radioactive source. For comparison, in the current study, which also simulated the results for the photon energy of a ^{137}Cs source, μ was $0.076 \text{ cm}^2 \text{ g}^{-1}$ (all soil horizons), HVL ranged from 6.10 cm (horizon (A)) to 6.44 cm (C2), TVL varied from 20.25 (A) to 21.40 cm (C2) and Z_{eff} varied from 10.27 (C1) to 10.31 (C2).

The clay fraction of the studied soil has the potential to be used for radiation shielding. Previous studies suggested that natural materials can be as effective for radiation shielding as conventional materials such as concrete and are therefore promising for shielding due to their low cost, abundance and ease of extraction (Mann *et al.*, 2013; Gülbiçim *et al.*, 2017). For lower photon

energies, blocks containing clay or clay mixtures may provide a viable alternative for radiation shielding (Mann *et al.*, 2016).

Conclusions

This study of a Brazilian Arenosol as a radiation shielding material yielded the following conclusions. The major oxides (Al_2O_3 , SiO_2 and Fe_2O_3) and the mineralogical composition do not differ significantly between the soil horizons. The mass attenuation coefficient and the effective atomic number of the horizons across the radiation energies did not differ significantly between the soil horizons. The proposed hypothesis was partially confirmed, as evidenced by the differences between the horizons, mainly for photon energies greater than 100 keV for MFP, HVL and TVL. The horizons with the greatest bulk densities exhibited the best shielding efficiencies. Overall, the surface horizon (A) demonstrated the most effective shielding results. This finding is evidenced by its lower MFP, HVL and TVL values compared with the other horizons. The effective atomic number was not a sensitive parameter for demonstrating differences between the horizons due to the slight variations in soil chemical compositions and mass attenuation coefficients. However, upon comparison of the results of this study with the previous scientific literature, it is evident that the clay fraction of the studied Arenosol is effective for shielding radiation. The presence of Fe and Al oxides in the clay fraction is fundamental to forming cohesive structures due to the clay minerals' ability to form aggregates. This factor makes the

clay fraction interesting as a material for attenuating radiation as denser clay structures are more efficient as radiation shielding materials. Another advantage of using clays is that extraction of a soil fraction can produce more affordable materials with the potential for use in radiation attenuation.

Acknowledgements. The authors thank the institutional laboratories FASCA/UEPG, GPMFE/UEPG, C-LABMU/UEPG, Coordination for the Improvement of Higher Education Personnel (Capes), Araucaria Foundation for Supporting Scientific and Technological Development of the State of Paraná (FA) and Brazilian National Council for Scientific and Technological Development (CNPq). LFP thanks CNPq for the research grant (304925/2019-5).

Financial support. This research was partially funded by the Coordination for the Improvement of Higher Education Personnel (CAPES – Coordenação de Aperfeiçoamento de Pessoal de Nível Superior; Grant 88882.450143/2019-01 and Finance Code 001) and Araucaria Foundation for Supporting Scientific and Technological Development of the State of Paraná (FA – Fundação Araucária de Apoio ao Desenvolvimento Científico e Tecnológico do Estado do Paraná; Grant 88882.168500/2018-01).

Conflicts of interest. The authors certify that they have no affiliations with or involvement in any organization or entity with any financial interest or non-financial interest in the subject matter or materials discussed in this manuscript.

Data availability. The datasets generated and/or analysed during the current study are available from the authors upon reasonable request.

Author contributions. Luiz F. Pires: Conceptualization, Formal analysis, Writing – original draft, Writing – review and editing. Victor A. Yanaguisawa: Formal analysis, Conceptualization, Investigation, Funding acquisition, Project administration, Resources, Writing – original draft. André M. Brinatti: Methodology, Formal analysis, Funding acquisition, Investigation, Project administration, Resources, Writing – original draft. Sérgio C. Saab: Project administration, Resources, Writing – original draft. Vladia Correchel: Project administration, Resources, Writing – original draft. All authors have read and agreed to the published version of the manuscript.

References

- Abdul A.T. & Rashid J.M. (2021) Experimental Investigation of gamma-ray shielding capability of clay used as building materials in Thi Qar Province. P. 012124 in: *Journal of Physics: Conference Series* (Vol. 1999, No. 1). IOP Publishing, Bristol, UK.
- AbuAlRoos N.J., Amin N.A.B. & Zainon R. (2019) Conventional and new lead-free radiation shielding materials for radiation protection in nuclear medicine: a review. *Radiation Physics and Chemistry*, **165**, 108439.
- Akbulut S., Sehhatigirdi A., Eroglu H. & Çelik S. (2015) A research on the radiation shielding effects of clay, silica fume and cement samples. *Radiation Physics and Chemistry*, **117**, 88–92.
- Akman F., Turan V., Sayyed M.I., Akdemir F., Kaçal M.R., Durak R. & Zaid M.H.M. (2019) Comprehensive study on evaluation of shielding parameters of selected soils by gamma and X-rays transmission in the range 13.94–88.04 keV using WinXCom and FFAST programs. *Results in Physics*, **15**, 102751.
- Al-Masri M.S., Hasan M., Al-Hamwi A., Amin Y. & Doubal A.W. (2013) Mass attenuation coefficients of soil and sediment samples using gamma energies from 46.5 to 1332 keV. *Journal of Environmental Radioactivity*, **116**, 28–33.
- Alabsy M.T. & Elzaheer M.A. (2023) Radiation shielding performance of metal oxides/EPDM rubber composites using Geant4 simulation and computational study. *Scientific Reports*, **13**, 7744.
- Azreen N.M., Rashid R.S., Haniza M., Voo Y.L. & Amran Y.M. (2018) Radiation shielding of ultra-high-performance concrete with silica sand, amang and lead glass. *Construction and Building Materials*, **172**, 370–377.
- Balan E., Lazzeri M., Morin G. & Mauri F. (2006) First-principles study of the OH-stretching modes of gibbsite. *American Mineralogist*, **91**, 115–119.
- Bish D.L. & Von Dreele R.B. (1989) Rietveld refinement of non-hydrogen atomic positions in kaolinite. *Clays and Clay Minerals*, **37**, 289–296.
- Bortoluzzi E.C., dos Santos D.R., Santanna M.A. & Caner L. (2013) Mineralogy and nutrient desorption of suspended sediments during a storm event. *Journal of Soils and Sediments*, **13**, 1093–1105.
- Camargo M.A., Kodum K.S. & Pires L.F. (2021) How does the soil chemical composition affect the mass attenuation coefficient? A study using computer simulation to understand the radiation-soil interaction processes. *Brazilian Journal of Physics*, **51**, 1775–1783.
- Camargo M.A., Kodum K.S. & Pires L.F. (2022) How does the soil chemical composition affect its cross-sections, effective atomic number and electron density? Computer simulation analysis to highlight the radiation-soil interaction processes. *Brazilian Journal of Physics*, **52**, 154.
- Costa J.C., Borges, J.A.R., Pires L.F., Arthur R.C.J. & Bacchi O.O.S. (2014) Soil mass attenuation coefficient: analysis and evaluation. *Annals of Nuclear Energy*, **64**, 206–211.
- Delage P., Cui Y.J. & Tang A.M. (2010) Clays in radioactive waste disposal. *Journal of Rock Mechanics and Geotechnical Engineering*, **2**, 111–123.
- dos Santos J.C.B.D., Le Pera E., Souza Júnior V.S.D., Corrêa M.M. & Azevedo A.C.D. (2017) Gneiss saprolite weathering and soil genesis along an east-west regolith sequence (NE Brazil). *Catena*, **150**, 279–290.
- Eke C. (2021) Investigation of gamma-ray attenuation properties of beach sand samples from Antalya, Turkey. *Arabian Journal of Geosciences*, **14**, 1–16.
- Eke C. (2022) The effect of soil depth on the radiation absorption parameters of soil samples. *Bulletin of the Russian Academy of Sciences: Physics*, **86**, 1391–1399.
- Ferraz E.S.B. & Mansell R.S. (1979) *Determining water content and bulk density of soil by gamma-ray attenuation technique*. University of Florida, Technical Bulletin no. 807. University of Florida, Gainesville, FL, USA, 51 pp.
- Ferreira T.R., Pires L.F., Brinatti A.M. & Auler A.C. (2018) Surface liming effects on soil radiation attenuation properties. *Journal of Soils and Sediments*, **18**, 1641–1653.
- Gedik S. & Baytaş A. (2015) Shielding of gamma radiation by using porous materials. *Acta Physica Polonica A*, **128**, 174–175.
- Gee G.W. & Bauder J.W. (1986) Particle size analysis. Pp. 383–412 in: *Methods of Soil Analysis Part 1. Physical and Mineralogical Methods*, 2nd edition (A. Klute, editor). Agronomy Society of America and Soil Science Society of America, Madison, WI, USA.
- Gili M.B.Z. (2023) Photon-shielding properties of alkali- and acid-treated Philippine natural zeolite. *Clay Minerals*, **58**, 258–266.
- Graf D.L. (1961) Crystallographic tables for the rhombohedral carbonates. *American Mineralogist*, **46**, 1283–1316.
- Gülbiçim H., Tufan M.Ç. & Türkan M.N. (2017) The investigation of vermiculite as an alternating shielding material for gamma rays. *Radiation Physics and Chemistry*, **130**, 112–117.
- Gurler O., Tumsavas Z. & Akar Tarim U. (2020) Gamma-ray attenuation study for the soils of Bursa, Turkey, in the energy range 59.5–1332.5 keV. *Iranian Journal of Science and Technology, Transactions A: Science*, **44**, 1161–1166.
- Hammer Ø., Harper D.A.T. & Ryan P. (2001) *Past: paleontological statistics software package for education and data analysis*. *Palaeontologia Electronica*, **4**, 1–9.
- Hartemink A.E., Zhang Y., Bockheim J.G., Curi N., Silva S.H.G., Grauer-Gray J. et al. (2020) Soil horizon variation: a review. *Advances in Agronomy*, **160**, 125–185.
- Hila F.C., Javier-Hila A.M.V., Sayyed M.I., Asuncion-Astronomo A., Dican G.P., Jecong J.F.M. et al. (2021) Evaluation of photon radiation attenuation and buildup factors for energy absorption and exposure in some soils using EPICS2017 library. *Nuclear Engineering and Technology*, **53**, 3808–3815.
- Hillel D. (2014) *Environmental Soil Physics: Fundamentals, Applications, and Environmental Considerations*. Elsevier Science, Amsterdam, The Netherlands, 800 pp.
- Howard C.J., Sabine T.M. & Dickson F. (1991) Structural and thermal parameters for rutile and anatase. *Acta Crystallographica*, **B47**, 462–468.
- Hubbell J.H. & Berger M.J. (1987) XCOM: *photon cross section on a personal computer*. US Department of Commerce, Gaithersburg, MD, USA, 32 pp.
- Hubbell J.H. & Seltzer S.M. (1995) *Tables of X-Ray Mass Attenuation Coefficients and Mass Energy-Absorption Coefficients 1 keV to 20 MeV for*

- Elements Z = 1 to 92 and 48 Additional Substances of Dosimetric Interest. National Institute of Standards and Technology, Gaithersburg, MD, USA. Retrieved from <http://physics.nist.gov/PhysRefData/XrayMassCoef/cover.html>
- Isfahani H.S., Abtahi S.M., Roshanzamir M.A., Shirani A. & Hejazi S.M. (2019a) Investigation on gamma-ray shielding and permeability of clay-slag mixture. *Bulletin of Engineering Geology and the Environment*, **78**, 4589–4598.
- Isfahani H.S., Abtahi S.M., Roshanzamir M.A., Shirani A. & Hejazi S.M. (2019b) Permeability and gamma-ray shielding efficiency of clay modified by barite powder. *Geotechnical and Geological Engineering*, **37**, 845–855.
- IUSS Working Group WRB (2022) *World Reference Base for Soil Resources*, 4th edition. International Union of Soil Sciences (IUSS), Vienna, Austria, 236 pp
- Kaplan I. (1963) *Nuclear Physics*. Addison-Wesley Publishing Company, Boston, MA, USA, 783 pp.
- Kucuk N., Tumsavaz Z. & Cakir M. (2013) Determining photon energy absorption parameters for different soil samples. *Journal of Radiation Research*, **54**, 578–586.
- Lima A.P.B., Inda A.V., Zinn Y.L., Silva E.R.D. & Nascimento P.C.D. (2022) Soil formation and properties along a sedimentary lithosequence in the eotonal cerrados of Mato Grosso, Brazil. *Catena*, **219**, 106599.
- Mamikhin S.V., Manakhov D.V., Shcheglov A.I. & Tsvetnov E.V. (2017) Some aspects of evaluation of the role of soils as a shielding medium from ionizing-radiation. *Moscow University Soil Science Bulletin*, **72**, 66–70.
- Mann H.S., Brar G.S., Mann K.S. & Mudahar G.S. (2016) Experimental investigation of clay fly ash bricks for gamma-ray shielding. *Nuclear Engineering and Technology*, **48**, 1230–1236.
- Mann K.S., Kaur B., Sidhu G.S. & Kumar A. (2013) Investigations of some building materials for γ -rays shielding effectiveness. *Radiation Physics and Chemistry*, **87**, 16–25.
- Mareschal L., Nzila J.D.D., Turpault M.P., Thongo M'Bou A., Mazoumbou J.C., Bouillet J.P. et al. (2011) Mineralogical and physico-chemical properties of ferralic Arenosols derived from unconsolidated Plio-Pleistocene deposits in the coastal plains of Congo. *Geoderma*, **162**, 159–170.
- Marquez-Mata C.A., Chavez M.J.M., Campillo-Rivera G.E., Vazquez-Bañuelos J., Garcia-Duran A. & Vega-Carrillo H.R. (2021) Shielding features of seven types on natural quartz. *Applied Radiation and Isotopes*, **167**, 109450.
- Medhat M.E., Demir N., Akar Tarim U. & Gurler O. (2014a) Calculation of gamma-ray mass attenuation coefficients of some Egyptian soil samples using Monte Carlo methods. *Radiation Effects and Defects in Solids*, **169**, 706–714.
- Medhat M.E., Pires L.F. & Arthur R.C.J. (2014b) Analysis of photon interaction parameters as function of soil composition. *Journal of Radioanalytical and Nuclear Chemistry*, **300**, 1105–1112.
- Mirji R. & Lobo B. (2017) Computation of the mass attenuation coefficient of polymeric materials at specific gamma photon energies. *Radiation Physics and Chemistry*, **135**, 32–44.
- Mudahar G.S., Modi S. & Makhan S. (1991) Total and partial mass attenuation coefficients of soil as a function of chemical composition. *International Journal of Radiation Applications and Instrumentation. Part A. Applied Radiation and Isotopes*, **42**, 13–18.
- Ngole-Jeme V.M. & Ekosse G.I.E. (2015) A comparative analyses of granulometry, mineral composition and major and trace element concentrations in soils commonly ingested by humans. *International Journal of Environmental Research and Public Health*, **12**, 8933–8955.
- Oliveira P.T.S., Nearing M.A., Hawkins R.H., Stone J.J., Rodrigues D.B.B., Panachuki E. & Wendland E. (2016) Curve number estimation from Brazilian cerrado rainfall and runoff data. *Journal of Soil and Water Conservation*, **71**, 420–429.
- Pires L.F. (2022) Radiation shielding properties of weathered soils: influence of the chemical composition and granulometric fractions. *Nuclear Engineering and Technology*, **54**, 3470–3477.
- Prandel L.V., Saab S.C., Brinatti A.M., Giarola N.F.B., Leite W.C. & Cassaro F.A.M. (2014). Mineralogical analysis of clays in hardsetting soil horizons, by X-ray fluorescence and X-ray diffraction using Rietveld method. *Radiation Physics and Chemistry*, **95**, 65–68.
- Şakar E., Özpolat Ö.F., Alım B., Sayyed M.I. & Kurudirek M. (2020) *Phy-X/PSD*: development of a user friendly online software for calculation of parameters relevant to radiation shielding and dosimetry. *Radiation Physics and Chemistry*, **166**, 108496.
- Schaefer C.E.G., Fabris J.D. & Ker J.C. (2008) Minerals in the clay fraction of Brazilian Latosols (Oxisols): a review. *Clay Minerals*, **43**, 137–154.
- Shultis J.K. & Faw R.E. (2005) Radiation shielding technology. *Health Physics*, **88**, 587–612.
- Silva V.E., Montanari R., Lima E.S., da Silva P.R.T., Freitas L.A., Pinotti C.R. et al. (2017) Liming influence on the spatial variability of the leaf chemical composition and in the initial growth of the Eucalyptus. *Journal of Geospatial Modelling*, **2**, 1–11.
- Singh V.P., Badiger N.M. & Kucuk N. (2014) Gamma-ray and neutron shielding properties of some soil samples. *Indian Journal of Pure and Applied Physics*, **52**, 579–587.
- Taqi A.H. & Khalil H.J. (2017) An investigation on gamma attenuation of soil and oil-soil samples. *Journal of Radiation Research and Applied Sciences*, **10**, 252–261.
- Tarim U.A., Gurler O.R.H.A.N., Ozmutlu E.N. & Yalcin S. (2013) Monte Carlo calculations for gamma-ray mass attenuation coefficients of some soil samples. *Annals of Nuclear Energy*, **58**, 198–201.
- Tech L., Pires L.F., Brinatti A.M., Saab S.C., Correchel V. & Momoli R.S. (2022) Elemental and radiation attenuation parameter analyses to characterize a Cambisol from the Serra Dourada State Park, Brazil. *Environmental Earth Sciences*, **81**, 63.
- Tsang C.F., Neretnieks I. & Tsang Y. (2015) Hydrologic issues associated with nuclear waste repositories. *Water Resources Research*, **51**, 6923–6972.
- Wechsler B., Lindsley D. & Prewitt, C. (1984) Crystal structure and cation distribution in titanomagnetites ($\text{Fe}_3\text{-xTi}_x\text{O}_4$). *American Mineralogist*, **69**, 754–770.
- Wei P.H. (1935) Die Bindung im Quarz. *Zeitschrift fur Kristallographie*, **92**, 355–362.
- Zachary D., Filep T., Jakab G., Ringer M., Balázs R., Németh T. & Szalai Z. (2023) The effect of mineral composition on soil organic matter turnover in temperate forest soils. *Journal of Soils and Sediments*, **23**, 1389–1402.